

Article

Not peer-reviewed version

Effects of Ammonia Mitigation on Secondary Organic Aerosol and Ammonium Nitrate Particle Formation in Photochemical Reacted Gasoline Vehicle Exhausts

[Hiroyuki Hagino](#) *

Posted Date: 26 July 2024

doi: 10.20944/preprints202407.2177.v1

Keywords: Volatile Organic Compounds (VOCs); Nitrogen Oxides (NO_X); Indoor Smog Chamber



Preprints.org is a free multidiscipline platform providing preprint service that is dedicated to making early versions of research outputs permanently available and citable. Preprints posted at Preprints.org appear in Web of Science, Crossref, Google Scholar, Scilit, Europe PMC.

Copyright: This is an open access article distributed under the Creative Commons Attribution License which permits unrestricted use, distribution, and reproduction in any medium, provided the original work is properly cited.

Disclaimer/Publisher's Note: The statements, opinions, and data contained in all publications are solely those of the individual author(s) and contributor(s) and not of MDPI and/or the editor(s). MDPI and/or the editor(s) disclaim responsibility for any injury to people or property resulting from any ideas, methods, instructions, or products referred to in the content.

Article

Effects of Ammonia Mitigation on Secondary Organic Aerosol and Ammonium Nitrate Particle Formation in Photochemical Reacted Gasoline Vehicle Exhausts

Hiroyuki Hagino * and Risa Uchida

Japan Automobile Research Institute (JARI), 2530 Karima, Tsukuba 305-0822, Ibaraki, Japan; urisa@jari.or.jp

* Correspondence: hhagino@jari.or.jp

Abstract: Gaseous air pollutants emitted from anthropogenic sources are diverse and form secondary products through photochemical reactions, complicating the regulatory analysis of anthropogenic emissions in the atmosphere. Here, we used an environmental chassis dynamometer and a photochemical smog chamber to conduct a parameter sensitivity experiment to investigate the formation of secondary products from a direct-injection gasoline passenger car. To simulate the mitigation of ammonia (NH_3) emissions from gasoline vehicle exhausts assuming future emission controls and to allow photochemical oxidation and aging of the vehicle exhaust, NH_3 was selectively removed by a series of five denuders installed between the vehicle and the photochemical smog chamber. Overall, there were no differences in the formation of secondary organic aerosols and ozone with or without NH_3 mitigation. However, the secondary particle formation potential of ammonium nitrate (NH_4NO_3) was significantly reduced with NH_3 mitigation. In addition, NH_3 mitigation resulted in increased particle phase acidity due to HNO_3 in the gas phase not being neutralized by NH_3 and condensing onto the liquid particle phase, indicating a potentially important secondary effect associated with NH_3 mitigation. The present study provides new insights into the effects of NH_3 mitigation on secondary emissions from gasoline vehicle exhaust and the experimental approach.

Keywords: volatile organic compounds (VOCs); nitrogen oxides (NO_x); indoor smog chamber

1. Introduction

Vehicle exhaust emissions are a major source of gaseous and particulate matter (PM) in the urban atmosphere. The recent regulatory landscape and electrification of vehicles have led to decreases of primary PM emissions released directly into the atmosphere via vehicle exhaust, such as elemental carbon (EC), primary organic aerosols (POAs), volatile organic compounds (VOCs), and nitrogen oxides (NO_x) [e.g., [1]]. However, there are still concerns about high ozone concentrations due to transboundary pollution, scattered localized high ozone (O_3) concentrations formation due to VOCs and NO_x [e.g., [2]]. Additionally, several studies have shown that secondary PM emissions, such as secondary organic aerosols (SOAs), are formed in the atmosphere by photochemical reactions of VOCs and NO_x contained in vehicle exhaust [3,4]. Because SOA produced from vehicle exhaust can be more toxic than SOA produced from VOCs from other sources or from POA produced from vehicle exhaust [5,6], a better understanding of the properties of SOA produced from vehicle exhaust is needed.

Although SOAs formed from vehicle exhaust are a major source of SOA in the atmosphere, their relative contribution varies considerably among studies. In modeling studies, gasoline vehicles have been reported to account for only 56–79% of SOA formed in the United States as a whole [7] but ≥90% in Southern California [8,9]. The relative contributions of diesel and gasoline vehicles to total vehicle

SOA is also unclear. For example, diesel vehicles are reported to contribute significantly to SOA in the atmosphere in the U.S. (around 90% of the total vehicle SOA) [10] and in London [11]. However, in a laboratory-based study, gasoline vehicles produced SOA, but diesel vehicles equipped with DPFs did not, suggesting that gasoline passenger cars make an important contribution to the SOA produced by vehicles in urban areas [12]. Thus, to be able to obtain accurate estimates of the contribution to environmental pollution of different sources of secondary products such as SOA, a deeper understanding of the characteristics of the secondary products from vehicle exhaust is needed.

The photochemical smog chamber is a useful tool for examining the formation and evolution of air pollutants under controlled conditions and to parameterize atmospheric processes and reveal their underlying mechanisms. However, generating realistic vehicle emissions under controlled and reproducible conditions also requires specialized test equipment (e.g., chassis dynamometers) that is usually not available in large stationary smog chambers. To overcome facility limitations, mobile smog chambers have been used to evaluate automotive emissions and the photochemical reactions they undergo in the atmosphere [12–16]. One area of research in which such mobile chambers have been used is in the investigation of the mechanisms of SOA formation and the effects that vehicle type (gasoline or diesel, year) [12–14,17,18], emission control technologies [20,21], driving conditions [22,23], and fuel type [24–27], have on SOA formation in vehicle exhaust, and collectively the results have demonstrated that SOA formation potentials vary significantly depending on the experimental parameters.

Evaluating the impacts of vehicle emissions on air quality requires consideration not only of photochemical reactions involving VOCs and NO_x, but also those involving ammonia (NH₃), which is a highly reactive alkaline inorganic gas that can negatively impact the environment [28–30]. Therefore, quantification of NH₃ emissions from vehicle exhaust is crucial for assessing air quality impacts and developing effective control strategies. The National Emission Ceilings Directive 2001/81/EC, the Gothenburg Protocol under the United Nations Convention on Long-Range Transboundary Air Pollution, and the Integrated Pollution Prevention and Control Directive (2008/1/EC) all aim to reduce emissions of NH₃ [29]. As the only alkaline inorganic gas with high reactivity, NH₃ is known to contribute to the formation of ammonium nitrate (NH₄NO₃) particles in automotive emissions [16,18,21,24,25,27]. However, since there is an overall sparsity of knowledge regarding the role of NH₃ in the formation of SOA in automotive emissions, more detailed investigations of potential impacts are needed.

As mentioned above, secondary pollution is caused by the formation of secondary particles and O₃. Previous studies of vehicle emissions based on photochemical smog chamber experiments have been limited in their assessment of both secondary particles and O₃. Therefore, in order to obtain the novelty of the study, it is necessary to evaluate the O₃ formation for modern vehicles in this study compared to previous studies.

Here, we used an environmental chassis dynamometer and a photochemical smog chamber to conduct a parameter sensitivity experiment to investigate the formation of secondary pollutants, both secondary particles and ozone, in exhaust from a direct-injection gasoline passenger car with or without NH₃ emissions mitigation.

2. Materials and Methods

2.1. Vehicle Chassis Dynamometer Experiments

Vehicle tests were performed in an environmental chamber with controlled temperature and humidity (23°C with 50% relative humidity control, 0°C without relative humidity control, or -7°C without relative humidity control) at the Japan Automobile Research Institute (JARI). The chassis dynamometer test facility within JARI complies with the World harmonized Light duty vehicle Test Procedure (WLTP) for type approval testing. The chamber contained a four-wheel drive chassis dynamometer for environmental-type experimental testing (Meiden, Japan) on which the test vehicle was placed. The exhaust pipe of the test vehicle was connected to a dilution tunnel (DLS-ONE-D; Horiba, Ltd., Kyoto, Japan,) and a constant volume sampler (12 m³/min; CVC-ONE-MV-HE(ESU); Horiba, Ltd., Kyoto, Japan). Exhaust gases were diluted an average of 24 times with high-efficiency

particulate air (HEPA). Background air filtered through an activated carbon and a HEPA filter was maintained at 298 K and 50% relative humidity. Carbon monoxide, carbon dioxide, NO_x, total hydrocarbons, and non-methane hydrocarbons were sampled near the end of the dilution tunnel, and their concentrations were measured with an exhaust gas analyzer (MEXA7200LE, Horiba, Ltd., Kyoto, Japan). EC and primary organic carbon (POC) were collected from the dilution tunnel onto a quartz filter (Pallflex, 2500QAT-UP, 47 φ ; Pall Corp., NY, USA) and determined by a thermal-optical carbon analyzer (model 2001; Desert Research Institute, NV, USA) using the IMPROVE protocol.

A small, direct-injection, two-wheel drive, gasoline passenger car of a size that is currently popular in Japan was tested (vehicle mass: 1340 kg, displacement: approx. 1.5 L, mileage: 23,192 km). Cold-start operational tests were performed based on the WLTC cycle of operation. For these cold-start experiments, the vehicle was warmed up by the same test cycle prior to the experiment and then left for approximately 23.5 h. The cold-start experiment was performed once a day.

2.2. Photochemical Smog Chamber

2.2.1. Facility

A mobile photochemical smog chamber [e.g., [12–16,31]], designed for the evaluation of secondary particle formation potential from automotive exhaust gases, was installed next to the environmental chassis dynamometer. The photochemical smog chamber comprised a fixed frame (2.08 m height \times 2.08 m width \times 2.66 m depth) fitted with casters, a reactor bag, and a light source. The reactor bag was made from a transparent, chemically inert, ultraviolet light (UV)-permeable, 54- μ m thick, fluorinated ethylene propylene (FEP) Teflon film. When fully filled with sample gas, the volume of the bag was 7.5 m³. The bag was fixed inside its own aluminum frame (1.5 m height \times 2 m width \times 2 m depth) and the frame was attached to the fixed frame of the smog chamber with a polytetrafluoroethylene gasket between the two frames such that the reactive gas contact area was not in contact with the aluminum frame. A reflector made of treated stainless steel (SUS304) was placed on the underside of the fixed frame, and 80 UV lamps (40 W, UVA340+; Q-Lab Corp. OH USA) were installed on the reflector with a sheet of FEP Teflon placed between the lamps and the reactor bag to prevent direct contact. The light transmission through FEP at wavelengths in the range of 290–800 nm is reported to be >90% [32,33]. The UV lamps were cooled by push-pull ventilation of the room air through 16 fans and exhausting it through 16 other fans.

2.2.2. Light Source

To trigger photolysis within the vehicle exhaust, particularly that of NO₂, which occurs at wavelengths <420 nm, the lights installed under the photochemical smog chamber were used to irradiate the reactor bag. A portable light spectrometer (USB2000 UV-VIS; Ocean Optics, Inc., USA) was used to characterize the irradiance spectrum reaching the inside of the reactor bag. The irradiance peaked at 350 nm, which was within the range of peak UV irradiances used in other indoor chamber-based studies (340–370 nm) [14,34–36]. Compared to the sunlight spectrum observed during the summer season in Tokyo, the installed lamps were found to be reproducing mainly the UV radiation between 295 and 320 nm.

The photolysis rate constant of NO₂ can be used to characterize irradiation intensity. In previous studies [34–37], the photolysis rate constant has often been calculated from the photolysis rate (J_{NO_2}) of NO₂ and steady-state concentrations of NO_x and O₃ [34,36,37]. However, in the present study, the J_{NO_2} of NO₂ was measured and the photolysis rates of several important species in atmospheric photochemistry were calculated; the J_{NO_2} values were obtained by NO_x and O₃ analyzers connected to the photochemical smog chamber under UV illumination from steady-state NO_x-O₃ concentrations. Using the NO₂ photolysis intensity determined from the zenith angle [34,36], our light source at 23°C (photolysis rate: 0.43/min) was comparable to an average morning at the summer solstice in Tokyo (0.46/min, N 35°41'22", E139°41'30") and at 0°C (photolysis rate: 0.31/min) to the transit time when the sun is due south at the winter solstice in Tokyo (0.33/min). Maximum values in previous studies typically range from 0.12 to 0.54/min [14,34,36], with the present values being close to the median

value of the other studies. At -7°C (photolysis rate: 0.2/min), our light source was comparable to an average morning at the time of the summer solstice in Sapporo, a city in the far north of Japan (0.16/min, N $43^{\circ}3'51''$, E $141^{\circ}30'49''$).

OH exposure is a factor that affects the concentration of SOA and SOA carbon/oxygen ratios [e.g., [18]]. OH exposure was determined by using equation (1):

$$\text{OH exposure} = -\frac{1}{k_{\text{OH}}} \left(\ln \frac{[\text{VOC}]_{\text{Final}}}{[\text{VOC}]_{\text{Initial}}} \right) \quad (1)$$

OH exposure (molecules/cm³/h) was calculated based on the average decay rate of toluene as measured by the gas chromatography with a flame ionization detector (GC-NMHC analyzer, GL Sciences Inc.). The average OH reactivity rate k_{OH} value of toluene (5.63×10^{-12} cm³/molecules/s at 298 K (25°C) [38]) and measurement errors in toluene were the potential sources of uncertainty in the estimation of OH exposure.

2.2.3. Instrumentation

A series of instruments was used to characterize the gas- and particle-phase emissions in the reactor bag. Particle number distribution was measured with a scanning mobility particle sizer (classifier model 3080 and condensation particle counter (CPC) model 3750; TSI, Inc., MO, USA). Particle mass was measured as a 1-h value with a beta-ray absorption PM densitometer (PM712; Kimoto, Osaka, Japan). Secondary particle formation was monitored either by a soot-particle time-of-flight aerosol mass spectrometer or an aerosol chemical speciation monitor (both Aerodyne, Inc. MA, USA). Secondary particles were quantified by collecting 1 m³ volume on a quartz filter (Pallflex, 2500QAT-UP, 47 φ ; Pall Corp., NY, USA) after the 5-hour reaction. Nitrate and ammonium ions in the particles collected by the quartz filter were determined by ion chromatography (Dionex Integron; Thermo Fisher Scientific Inc., MA, USA). Organic carbon (OC) and EC collected on the quartz filters were determined by a thermal-optical carbon analyzer (model 2001; Desert Research Institute, NV, USA) using the IMPROVE protocol.

Gas-phase organic species in a reaction bag were monitored using a proton transfer reaction mass spectrometer (PTR-TOF 8000; Ionicon, Innsbruck, Austria). The gas-phase organic species were collected into a 5-L vinyl alcohol polymer bag (Smart Bag PA-AAK-5; GL Sciences Inc., Saitama, Japan) for before and after the photochemical reaction, and were determined by a gas chromatograph equipped with a flame ionization detector (model GC-NMHC, GL Sciences Inc.) for the analysis of non-methane hydrocarbons with carbon numbers between 2 and 12. Gas monitors were used to determine the concentrations of CO₂, NO_x-NH₃, and O₃ (Models 410i, 17i, and 49i, respectively; Thermo Fisher Scientific Inc., MA, USA); the monitors were zeroed daily and calibrated at least weekly. The concentration of HNO₃ gas and the acidity (H⁺ (aq)) formed in the aqueous liquid phase (aq) of the particles were obtained by calculation due to facility limitations. The concentration of HNO₃ gas was approximated from O₃ and HNO₃ concentration curves for the photochemical smog chamber obtained by using the Statewide Air Pollution Research Center chemical reaction model [39]. Acidity (H⁺ (aq)) was determined by using the ISORROPIA thermodynamic equilibrium model [40].

2.2.4. Experimental Procedures

It shows a summary of the process of injecting the exhaust gas into the photochemical smog chamber, performing photochemical oxidation and aging, measuring the sample gas, and cleaning the chamber after the experiment.

It shows a photograph of the experimental chamber with the test vehicle placed on the environmental chassis dynamometer. The vehicle exhaust was connected to the photochemical smog chamber via an ejector dilutor without (base scenario) or with a denuder line connected between the ejector dilutor and photochemical smog chamber. The exhaust gas was injected by the ejector diluter (dilution ratio: 12 times; DI-1000; Dekati Ltd., Kangasala, Finland) into the reactor bag of the portable smog chamber at a rate of 4.2 L/min. To supply the dilution gas with a constant flow rate into the reactor bag, clean air was supplied to the ejector diluter at 50 L/min under the control of a mass flow

controller (MQV0050; Azbil Corp., Tokyo, Japan). During a 30-min WLTC cycle, 1.625 m³ of dilution gas was introduced into the reactor bag; therefore, before injecting the exhaust gas into the photochemical smog chamber, suction was used to reduce the volume of the reactor bag by approximately 2 m³. As an additional hydroxyl radical (OH) source when adding the exhaust, H₂O₂ (0.25 mL, 30% v/v, 5 ppm equivalent in the reactor in our experiments) was also injected into the reactor bag via the make-up air supplied at 5 L/min [16,21,41]. The air supplied to the reactor bag was dry, but the exhaust gas contained moisture; at 23°C the relative humidity inside the reactor bag was <13%, at 0°C <34%, and at -7°C <43%.

Clean air was generated by an oil-free scroll compressor equipped with a membrane air dryer (SLP-221CD; Anest-Iwata Corp., Kanagawa, Japan); the dehumidified, compressed air was passed through a manual air dryer (model 4001; CKD, Aichi, Japan), an oxidation catalyst heated to 350°C, Purafil chemical adsorbents (Purafil and Purafil Puracarb AM; Purafil Inc., GA, USA) [36], activated carbon, and a molecular sieve, and finally through a HEPA filter.

The difference between the pressure in the reactor bag and the atmospheric pressure was monitored by a differential pressure gauge (GC62; Nagano Keiki Co. Ltd., Japan), and the mass flow controller automatically stopped the air supply when the pressure was ≥5 Pa, thus ensuring a constant reactor bag volume. After receiving the exhaust gas, the reactor bag was allowed to stand for 15 min to allow mixing. To allow determination of the gas concentrations in the exhaust prior to the photochemical reaction, 5 L of sample gas was collected into a Smart Bag PA and an aldehyde cartridge (InertSep mini AERO DNPH-HR; GL Sciences Inc., Saitama, Japan) over a 20-min period.

To obtain NH₃-free exhaust gas, NH₃ was selectively removed by installing a series of five stainless steel concentric tube denuders (DN-315; Sunset Laboratory Inc., OR, USA) between the ejector dilutor and the photochemical smog chamber. The inner wall of the denuder was impregnated with 10% malic acid in ethanol that was allowed to dry before use. The NH₃ collection efficiency of the series of experiment was 85% at 23°C, 98% at 0°C, and 98% at -7°C by calculating the NH₃ concentration in the reactor bag compared to without the denuder line.

UV light irradiation was started at about 2-hour after the exhaust gas from one WLTC run was started to inject into the photochemical smog chamber. The irradiation duration was 5-h, which corresponds to the average daily solar irradiation duration in Japan. During the UV irradiation, the instruments described in Section 2.2.3 collected samples of gas from the reactor bag and continuously measured their concentrations. The volume of the reactor bag was maintained by introducing clean air as make-up gas at 5 L/min; 25% dilution was achieved during the 5-h photochemical reaction.

Immediately after the end of the photoreaction period, 5 L of sample gas was collected in a Smart Bag PA and an aldehyde cartridge over a 20-min period. The sample gas was collected in the Smart Bag PA while mixing at 20 mL/min of 10 ppm nitric oxide and in the aldehyde cartridge with a potassium iodide cartridge with a potassium iodide cartridge in series in front to avoid reactions with the O₃ collection device and analyzer, respectively. Particles in a reaction bag after 5-h photochemical reaction were collected on a quartz filter with a volume of 1.00 m³ at a flow rate of 50 L/min by a pump with mass flow control, and secondary particles were quantified by measuring the concentrations of ionic components (NO₃⁻, NH₄⁺), OC, and EC.

2.2.5. Data analysis

Emission factors (EF_c) for the aerosols and gases detected in the reactor bag were calculated using the following equation and are reported as mass per mass of fuel burned (mg/kg-fuel):

$$EF_c = \frac{[C]}{[CO_2]} \times EF_{CO_2} \quad (2)$$

where [C] is the background- and dilution-corrected concentration of the gas or aerosol compositions in mg/m³, [CO₂] is the background- and dilution-corrected concentration of CO₂ in the chamber in g/m³; and EF_{CO₂} is the emission factor of CO₂ measured by a gas analyzer with the dilution tunnel shown in Section 2.1 in g/kg-fuel. The emission factors for SOA (secondary aerosol), NH₄NO₃, and NH₃ (primary gas) were determined from the concentrations in the smog chamber. The emission

factors for EC and primary organic carbon (POC) (primary aerosols) and NO_x and NMHC (primary gases) were determined from the concentrations in the dilution tunnel.

To quantify O₃ and HNO₃ gas formation in the smog chamber, we corrected for the rate of dilution air introduced into the smog chamber (0.04/h). To quantify secondary organic aerosol and NH₄NO₃ particle formation in the smog chamber, we corrected for the loss of aerosol particles to the reactor bag walls. Briefly, aerosol particle loss to the bag walls was treated as a first-order process with rate constants determined from decay measurements of inert tracer species (black carbon or sulfate seed) [42]. An aerosol particle wall loss rate constant without dilution was calculated using black carbon that is not lost due to reaction but only decays in concentration through dilution or wall loss, measured on a microAeth black carbon monitor (model MA350; AethLabs, CA, USA) [43]. Smog chambers with near-spherical surface volume ratios have the lowest aerosol particle wall loss rate constants [44], and compared to previous studies (e.g., 0.46 to 0.66 /h [e.g., [45]]), the aerosol particle wall loss rate constant in the present study (0.12/h) was smaller.

For the quantification of SOA, the most common measurement, secondary organic carbon (SOC), was quantified as organic carbon (OC) [46–48], which was collected on a quartz fiber filter and quantified by a thermal-optical carbon analyzer. The conversion of OC, where only carbon was quantified, to organic aerosol, which also contains carbon and hydrogen and oxygen, was performed by multiplying OC by a constant conversion factor, the organic mass-to-organic carbon (OM/OC) ratio, to estimate the total amount of SOA and POA [46] in equation (3):

$$EF_{SOA} = EF_{SOC} \times OM/OC_{SOA_T} - EF_{POC} \times OM/OC_{POA_T} \quad (3)$$

where OM/OC_{SOA_T} is the OM/OC ratio of OA containing mainly SOA and some POA in the chamber after the photochemical reaction, as observed by soot-particle time-of-flight aerosol mass spectrometry that is a standard high resolution time-of-flight aerosol mass spectrometer (HR-ToF-AMS) allowed to analyze elements in organics [47–49] coupled with a diode-pumped, Nd:YAG, intracavity, 1064-nm infrared laser vaporizer. The OM/OC ratios obtained were 1.8 at -7°C, 2.0 at 0°C, and 2.2 at 23°C. OM/OC_{POA_T} is the OM/OC ratio including only POA, also observed by HR-ToF-AMS, and the value was 1.2 at all three temperatures. Our OM/OC ratio values are consistent with the OM/OC ratio of 1.2 for POA reported for gasoline vehicles (1.2) [48], 2.0 reported from smog chamber experiments [48], and the range of 1.7 ± 0.5 for Southern California atmosphere [49]. Further investigations are needed to discuss the suitability of the OM/OC ratios used in our experiment, and this study only uses it as an empirical coefficient.

3. Results and Discussion

3.1. Primary Gas and Particle Emissions

It shows a comparison of emission results from the present study versus previously published data. For the gasoline vehicle tested under the WLTC mode in the present study, the emission factors at 23°C for NMHC (161–187 mg/kg-fuel) and NO_x (97–116 mg/kg-fuel) were generally lower than those reported from previous studies; NMHC and NO_x emissions in previous studies were in rather large ranges of 4–34980 mg/kg-fuel and 34–21970 mg/kg-fuel, respectively [14,15,24,27,50].

In general, gasoline vehicle emissions contribute more to final pollutant emissions during cold starts in cold environments than at room temperature [15,21,22]. This is because the engine and drive-related systems take time to stabilize, and the aftertreatment system needs time to reach its optimum activation temperature. Several previous studies have highlighted the need to consider the effects of low-temperature environments when evaluating emissions and air pollution [15,21]. The present emission factors for the low-temperature environments were 521–562 mg/kg-fuel for NMHC and 107–119 mg/kg-fuel for NO_x at 0°C, and 763–1210 mg/kg-fuel for NMHC and 89–97 mg/kg-fuel for NO_x at -7°C. At these low temperatures, the NMHC emissions exceeded those of the 23°C environment, whereas there was no marked change in NO_x emissions. These emission levels were similar to those observed for gasoline vehicle emissions in previous study where NMHC emissions were in the range of 1676–2064 mg/kg-fuel at 22°C and 5362–5778 mg/kg-fuel at -7°C, and NO_x emissions were in the range of 123–131 mg/kg-fuel at 22°C and 384–408 mg/kg-fuel at -7°C [24].

Secondary pollution is suggested to occur when NH_3 reacts with nitrogen oxides in the atmosphere to form NH_4NO_3 [21,24,25,27,50]. For the gasoline vehicle used in the present study, the emission factor for NH_3 was in the range of 25–28, 25–40, and 23–73 mg/kg-fuel at 23°C, 0°C, and -7°C, respectively. Thus, NH_3 emissions tended to be greatest at -7°C. Previous studies have reported NH_3 emissions with considerable variation, ranging from 4 to 3206 mg/kg-fuel at 23°C.

In interpreting these results it is important to consider the causes of the large variations in the reported values. Factors contributing to these large variations include regulatory age [12–14,17], engine maintenance history, and the type of aftertreatment equipment installed on the vehicle [20,21]; thus, it is important to note the likelihood of individual vehicle effects when interpreting the results.

3.2. Primary and Photochemical Reacted Exhaust

It shows the PM composition (sum of primary emissions and secondary formation potentials as emissions) in the diluted exhaust gas after it was subjected to UV irradiation for 5 h. The graph also summarizes the primary emissions of NMHC, NO_x , and NH_3 , and the secondary formation potentials of SOA, NH_4NO_3 , acidity in aerosols, and O_3 , in order to allow comparison of overall emissions, including primary emissions and secondary formation potentials.

The repeatability of the particle mass composition measurements ($n = 2$) at 23°C was 9.3% for EC, 5.6% for POA, 11.0% for SOA, 13.4% for NH_4NO_3 , and 5.1% for O_3 ; at 0°C it was 37.7% for EC, 72.0% for POA, 7.6% for SOA, 24.9% for NH_4NO_3 , and 30.0% for O_3 ; and at -7°C it was 42.8% for EC, 9.9% for POA, 58.2% for SOA, 7.7% for NH_4NO_3 , and 14.1% for O_3 .

The emission percentages of the particle mass composition varied slightly with temperature, with the secondary particles, ammonium nitrate (79.6% at 23°C, 58.8% at 0°C, and 38.3% at -7°C) and SOA (19.2% at 23°C, 35.7% at 0°C, and 47.5% at -7°C), comprising 79.6%, 58.8%, and 38.3% of the particles, respectively. The primary particles, EC, POA, and POA were 0.8%, 4.0%, and 12.3% at 23°C, 0°C, and -7°C, respectively, and 0.4%, 1.5%, and 1.9% at 23°C, 0°C, and -7°C, respectively.

The PM composition after UV irradiation varied with temperature. Among the primary particles, EC accounted for 0.8%, 5.4%, and 12.3% of the total PM composition at 23°C, 0°C, and -7°C, respectively, and POA accounted for 0.4%, 1.3%, and 1.9%, respectively. Among the secondary particles, NH_4NO_3 accounted for 79.6%, 46.7%, and 38.3% of the total PM composition at the three temperatures, and SOA accounted for 19.2%, 46.6%, and 47.5%, respectively. Thus, the majority of aerosols remaining after photochemical reaction were secondary aerosols of NH_4NO_3 and SOA. Overall, the primary particles accounted for only 1.2%, 6.7%, 14.2% of the total PM at 23°C, 0°C, and -7°C, respectively.

Recent emission controls targeting primary particles have generally been based on worst-case scenarios such as under conditions of very low temperature (e.g., -7°C) [e.g., [51]]. However, the present findings show that when secondary particles formed by atmospheric photochemical reactions are considered, the worst-case scenario for total PM emissions is actually at 23°C, and that under this scenario the PM emissions are dominated by secondary particles. Additionally, our results indicate that NH_3 mitigation resulted in significant acidity (H^+) formation in the low-temperature environment. Further studies are needed to elucidate the impacts of vehicle type and humidity conditions on the secondary particle composition of vehicle exhaust.

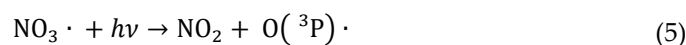
3.3. Effects of Ammonia Mitigation

3.3.1. NH_4NO_3 Particle Formation

NH_3 mitigation by using a series of five NH_3 denuders had a marked effect on the amount of secondary NH_4NO_3 particles formed during UV irradiation. Without NH_3 mitigation, NH_4NO_3 particles were emitted at 208 ± 28 , 74 ± 12 , and 49 ± 4 mg/kg-fuel at 23°C, 0°C, and -7°C, respectively, whereas with NH_3 mitigation the emissions were 2, 3, and 19 mg/kg-fuel, respectively, which was a considerable reduction. Thus, the NH_3 removal efficiency of the series of denuders was 85% at 23°C, 98% at 0°C, and 98 at -7°C, and the reduction of NH_4NO_3 particle formation was 99%, 96%, and 61% at 23°C, 0°C, and -7°C, respectively. These findings show that although NH_3 mitigation was effective

at reducing NH_4NO_3 particle formation, the reduction was not necessarily linear with environmental temperature. In addition, although we do not yet have a complete explanation for the discrepancy between the collection efficiency of the denuders and the reduction rate of NH_4NO_3 particle formation, we consider that it is likely due to the rather complicated chemical equilibrium of NH_4NO_3 particle formation, as described below.

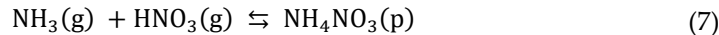
NH_4NO_3 is formed when nitric acid (produced by the oxidation of NO_x) reacts homogeneously with gaseous NH_3 . It has been noted that the secondary formation of NH_4NO_3 from gasoline vehicle emissions is due to the presence of NH_3 and NO_x in the emissions [52]. It is also known that nitrate radicals (NO_3) and dinitrogen pentoxide (N_2O_5) are involved in the formation of nitric acid (HNO_3) gas from NO_x [53]. The rate of photolysis of NO_3 radicals by visible light (wavelength 420–690 nm) is about 10 times faster than that of nitrogen dioxide; therefore, the atmospheric NO_3 radicals concentration is very low during the daytime (i.e., under conditions involving visible light) [54].



Recently, however, it has been found that marked amounts of nitrate are present during the evening and morning twilight hours, and occasionally during the day when light levels are low [55]. Studies assessing the importance of this nitrate radical generation during the day have also been published [56,57]. During the night, NO_3 radical is produced by the reaction of NO_2 with O_3 ; NO_3 radical reacts with NO_2 to produce N_2O_5 , and the produced N_2O_5 then reacts with liquid water droplets on aerosol particles to produce HNO_3 :



When HNO_3 is present in the atmosphere, it tends to react with basic species such as NH_3 gas. The neutralization reaction between $\text{NH}_3(\text{g})$ and $\text{HNO}_3(\text{g})$ to form NH_4NO_3 particles ($\text{NH}_4\text{NO}_3(\text{p})$) is reversible and is considered the main source of particulate nitric acid aerosols ($\text{NH}_4\text{NO}_3(\text{p})$) in urban air [58]. The reaction is as follows:



The equilibrium constant for the reaction in equation (7) depends on the gas concentration, relative humidity, and temperature [59–61]. The formation of particulate NH_4NO_3 is enhanced under conditions of high gas concentration, high relative humidity, and low temperature [60]. Aqueous ammonium nitrate exhibits temperature dependence, and the amount of particulate ammonium nitrate is determined from the amount above the equilibrium concentration of HNO_3 and available NH_3 . Aqueous NH_4NO_3 also exhibits a temperature dependence, and the amount of particulate NH_4NO_3 is determined from the concentration of HNO_3 and NH_3 above the equilibrium of equation (7). Only NH_4NO_3 particles tended to be reduced by selective NH_3 mitigation; the reason is that the equilibrium reaction is not established due to the elimination of NH_3 gas on the left side of equation (7).

It shows a contour map of the emission coefficients of NH_4NO_3 particles formed in the equilibrium reaction in equation (7) versus the emission coefficients of HNO_3 and NH_3 gases. The contour plots for NH_4NO_3 particles were calculated in ISORROPIA [40] using the concentrations of HNO_3 and NH_3 precursor gases for the NH_4NO_3 particles, converted to emission factors and plotted. The equilibrium constant for the reaction in equation (6) shows that the formation of NH_4NO_3 particles is less temperature-dependent when the emissions of HNO_3 and NH_3 are sufficiently high. In the present study, when NH_3 mitigation was used, the concentration of NH_3 was reduced, and thus the formation of NH_4NO_3 particles was reduced at both temperature conditions of 23°C, 0°C, and -7°C compared to the base scenario without NH_3 mitigation. Compared to at 23°C, the HNO_3 concentration produced from NO_x emissions at 0°C and -7°C tended to decrease due to a slowing of the photochemical reaction. The measured value of the NH_4NO_3 particle agrees with the calculated value if it is the same color as the background contour map. Not all plots matched the calculated

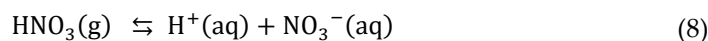
values, tending to be slightly overestimated at 23°C and slightly underestimated at 0°C and -7°C. In this study, the concentration of HNO₃ gas was not directly measured, and NH₃ gas is generally quite difficult to accurately measure due to its sticky nature. Therefore, the consistency with the calculated (color scheme in contour maps) and observed (color scheme in plots) NH₄NO₃ values may be attributed to experiments based on limited resources for measuring the precursor gas NH₃ and calculating HNO₃. Further research should clarify the consistency with the calculated and observed NH₄NO₃ values based on highly sensitive and accurate measurements of the precursor gases. Regardless, our experiments indicate that selective NH₃ mitigation using NH₃ denuders tended to reduce NH₄NO₃ particles in relative to without NH₃ mitigation.

Since the HNO₃ concentration was lower at the lower temperatures, the trend of increasing acidity (H⁺) due to NH₃ removal also tended to be less at lower temperatures. Given that the aerosol formation potential was evaluated under dry conditions in the present study, further studies are needed to evaluate changes in the NH₄NO₃ particle formation potential and acidity (H⁺) due to NH₃ removal in relation to humidity.

It has been reported that the increase in NH₄NO₃ mass after photochemical reaction of gasoline vehicle exhaust is due more to the presence of NH₃ than to a reduction in NO_x emissions [21,52]. Gasoline particulate filters (GPFs) with catalysts, an aftertreatment device for gasoline vehicles, are reported to reduce NO_x emissions from the tailpipe by 16.6% [21] or 87.6% [52], but it has been reported previously that more NH₄NO₃ was produced in the photochemical smog chamber than in an experiment without GPFs [21]. Overall, the role of NH₃ in gasoline direct-injection vehicles with and without GPFs should be further investigated, as NH₃ may contribute significantly to the formation of secondary inorganic aerosols, primarily in the form of NH₄NO₃. NH₃ can also be produced in three-way catalysts from NO_x emitted from the engine and H₂ produced through water-gas shift and hydrocarbons steam reforming reactions [62,63]. Such NH₃ is known to pass through GPF systems or be oxidized to N₂O, NO_x, or N₂ [62,63]. To address this, three-way catalysts are usually coated with precious metals such as Pt, Rh, or Pd on a ceramic or metal substrate. In general, Rh reduces NO_x, whereas Pd or Pt oxidizes CO and CH₄ emissions [64]. The composition of the catalytically active metal, the air/fuel ratio, and the operating temperature all play important roles in the formation of NH₃, which itself is a factor in the secondary formation of NH₄NO₃ particles, and of N₂O, a global warming potential. Also, catalysts with Pd/Rh or Pt/Rh as active metals produce NH₃ [65,66] and N₂O [67]. In the present study, we did not evaluate the differences in the amount of NH₄NO₃ particles formation potentials relative to differences in NH₃ emissions. However, it is reasonable to assume that the difference in the ratio of NH₄NO₃ particles to overall PM between the previous study [21,52] and our study was most likely the cause of the difference in the amount of NO_x and NH₃ in the tailpipe detected in the present study.

3.3.2. Acidity Formation

Less total PM emissions (sum of primary and secondary particles) were observed with NH₃ mitigation compared to without. These lower total PM emissions are attributed to the fact that with NH₃ mitigation, the nitric acid gas produced by the oxidation of NO_x reacts uniformly with the NH₃ gas to neutralize it and produce fewer NH₄NO₃ particles; with NH₃ removal, the nitric acid gas condenses onto liquid particles (aq: particles in the liquid phase), forming acidity (H⁺ (aq)) (i.e., forming the net of Equations. (8) and (9)):



The acidity (H⁺ (aq)) showed an increasing trend with NH₃ mitigation, but no change in nitrate gas formation was obtained. The decrease in NH₄NO₃ and the increase in acidity confirm that no neutralization reaction between nitrate and NH₃ gases occurred. Less HNO₃ gas was produced with decreasing temperature due to a decrease of OH exposure (6.1 × 10⁷ at 23°C, 3.3 × 10⁷ at 0°C, and 1.9 × 10⁷ molecules/cm³/h at -7°C), indicating a slowdown in the progress of the atmospheric oxidation

reaction. The removal efficiency of NH_3 gas was 85%, 98%, and 98% at 23°C, 0°C, and -7°C, respectively. Although there was a small amount of NH_3 gas remaining at 23°C, it was neutralized such that there was no marked increase in acidity (H^+). These findings suggest that a small amount of residual NH_3 gas can be neutralized, but that excessive NH_3 mitigation promotes acidification. Further studies are needed to assess the human health effects of such increased acidity, as well as the effects on air quality, rainfall, soil, and vegetation.

3.3.3. SOA Formation

No marked difference in SOA formation potential was observed with NH_3 mitigation. Without NH_3 mitigation, SOA was emitted at 50.2 ± 5 , 73.8 ± 1 , and 61.1 ± 36 mg/kg-fuel at 23°C, 0°C, and -7°C, respectively, whereas with NH_3 mitigation it was emitted at 63.3, 78.9, and 42.5 mg/kg-fuel, respectively. The effect of NH_3 on SOA formation has been demonstrated by previous photochemical smog chamber experiments and model analyses, showing that ammonium salts formed by the reaction of NH_3 with organic acids in SOA derived from styrene and α -pinene cause an increase of SOA formation [68], and that NH_3 competes with aldehydes to reduce the yield of secondary ozonides, which decreases SOA formation [69,70]. Although the organic acids and ozonides in photochemically reacted gasoline vehicle exhaust were not quantified in the present study, it is unlikely that they would have an effect on the reaction dependent on the presence of NH_3 . It is reasonable to assume that the differences in the values of SOA formation due to NH_3 mitigation obtained in this study was due to experimental variability given the limited number of experiments.

The trend of SOA formation can be quantified in terms of effective SOA yield (Y), defined as the measured SOA mass divided by the mass of SOA precursors reacted. Since SOA yields vary widely among VOC components [71,72], only a portion of NMHC emissions are SOA precursors. Due to the limited number of laboratory studies available in the literature, SOA production data are not available for all precursors. Although SOA yields remain a subject of debate, presenting the data as SOA yields accounts for differences in SOA production across experiments. Our estimates of SOA yields (0.372–0.866) varied but were comparable to previously reported values (0.07–0.9) [e.g., [24]]. SOA yield (Y) has been shown to be a function of SOA concentration (M_o) according to a classical model [73–75], and the relationship is described as follows:

$$Y = M_o \sum \left(\frac{\alpha_i K_{om,i}}{1 + K_{om,i} M_o} \right) \quad (10)$$

where $K_{om,i}$ and i are the mass-based gas-particle equilibrium partition coefficient and stoichiometric coefficient of product i , respectively, and M_o is the total mass concentration of organic matter (mg/m³). “ M_o ” is a common notation in previous studies, but M_o was obtained in this study by multiplying the dilution- and particle loss-corrected OC concentrations observed in the reaction bag after 5-h of photochemical reaction by the OM/OC_{SOA_T} ratio used in equation (3). Our effective SOA yield estimates varied considerably, but they plotted roughly backwards and forwards on the SOA yield curves for each environmental temperature (23°C, 0°C, and -7°C). With NH_3 mitigation, the obtained SOA yields may be judged as deviating somewhat from the SOA yield curve obtained for the 0°C condition; however, based on the relationship between the NMHC and SOA formation potentials, it is reasonable to interpret this as simply the variation obtained from the series of experiments. The relationship between SOA yield and temperature remains a subject of debate, with reports of both higher [12] and lower [24] SOA yields under low-temperature conditions for SOA produced from gasoline vehicle exhaust. Considering a gas-particle equilibrium based on the concept of effective evaporation enthalpy of a liquid becoming a gas [e.g., [76,77]], the higher SOA yield at low temperatures is considered to be a natural phenomenon in which less volatile gases condense into the particle phase, leading to more particle formation.

Our estimated yield of SOA at 23°C was higher compared to previous reported values (lower SOA yields of 0.07–0.7 with lower OH exposure of $0.1\text{--}1.5 \times 10^7$ molecules/cm³/h), which we attribute to a higher OH exposure (higher SOA yields of 0.731–0.866 with higher OH exposure of $6.0\text{--}6.3 \times 10^7$ molecules/cm³/h), and many studies support a higher SOA yield with higher OH exposure [e.g., [20]].

In the present study, we found that the lower the temperature, the lower the OH exposure. We believe that the lower SOA yield at lower temperatures is due to there being less SOA formation as a result of a slowing of the oxidation process. Consequently, our data indicate that the higher NMHC emissions at low temperatures (0°C and -7°C), which are often used as worst-case scenarios for atmospheric environmental policymaking, did not lead to the greatest SOA formation potential. We also suggest that the reduction of NH₃ did not lead to a reduction in SOA formation. However, we would like to emphasize that the actual experimental data suggest that the yield of SOA formed from gasoline vehicle emissions is also highly dependent on environmental temperature conditions.

3.3.4. O₃ Formation

No marked differences in O₃ emissions were observed with NH₃ mitigation. Without NH₃ mitigation, O₃ was emitted at 1053 ± 53, 553 ± 48, and 239 ± 34 mg/kg-fuel at 23°C, 0°C, and -7°C, respectively, whereas with NH₃ mitigation it was emitted at 1093, 585, and 234 mg/kg-fuel, respectively. The effect of NH₃ on O₃ formation can be evaluated through compound-limited photochemical smog chamber experiments; however, few such studies exist in the literature. In one study, a photochemical smog chamber was used to investigate the effect of NH₃ on secondary aerosol formation by photooxidation of toluene and NO_x under different O₃ formation regimes, and the study showed that although NH₃ concentration does not affect O₃ formation, it does affect secondary particle formation and composition [78].

O₃ formation potential (OFP) index, which quantifies the relative impact of individual VOCs on O₃ formation, has been widely used to help develop cost-effective ground-level ozone pollution control strategies [79,80]. For a given VOC or VOC mixture, OFP is determined by using maximum incremental reactivity (MIR) index [79–90]. MIR is defined as the gram of change in O₃ per gram of VOC defined as the O₃ change caused by the reaction of a quantity of VOC. The MIR index was developed using the Statewide Air Pollution Research Center (SAPRC) chemical reaction model built on a semi-explicit chemical mechanism [81,82,89,90]. Generally, the calculation of OFP index uses MIR index developed under high NO_x conditions, thus limiting the O₃-forming region to conditions where VOC concentrations are limited or at least VOC and NO_x mixing is limited [83]. For most studies of gasoline vapor emissions and gasoline vehicle emissions with low NO_x emissions [e.g., 80,84–88], however, OFP index have been derived by multiplying MIR index by observed VOC emission factors. Thus, the OFP index (mg-O₃/kg-fuel) of emitted NMHC can be calculated using the MIR index [89,90] and Equation (11):

$$\text{OFP index} = \sum \text{MIR}_i \times C_i \quad (11)$$

where MIR_i is the maximum incremental reactivity of VOC composition *i* (mg-O₃/mg-VOC), and C_i is the emission factor [mg/kg-fuel] of VOC composition *i* (VOC type: alkanes, alkenes, aromatics, aldehydes).

It shows a comparison of the OFP index (calculated by VOC concentration in the reaction bag) and O₃ formation potentials as emissions (measured in a reaction bag); the percentage contributions of alkenes and aromatics to the OFP are also indicated. In general, alkenes, aromatics, and aldehydes contribute more to higher MIR index [88]. In the present study, alkenes contributed 31%, 35%, and 33% to the OFP index at 23°C, 0°C, and -7°C, respectively, aromatics contributed 40%, 43%, and 47%, respectively, whereas aldehydes contributed 12%, 4.3%, and 1.7%, respectively. The distribution of the alkenes and aromatics did not change significantly with ambient temperature. There was almost no change in the contribution of VOC categories to OFP index due to NH₃ removal. The calculated OFP index results are interpreted as representative of the relative O₃ formation potential as emissions from different fuel compositions. They do not suggest the possibility of changing ozone concentrations in urban areas [86]. In the present study, the OFP index does not agree in trend with the O₃ formation potential; assessment by OFP index generally requires the use of detailed atmospheric chemistry models that account for many important additional factors (such as local meteorology and all sources of ozone precursors) [86]. Because the present study is too small in scope (i.e., single vehicle and single fuel type), we cannot conclude that the observations conclusively

explain the performance of the technologies considered. However, the present observations contribute to our understanding of the potential for changes in the composition of vehicle emissions to have a positive effect on the suppression of atmospheric ozone formation. That is, our findings emphasize that the ratios of VOCs contributing to the OFP index were largely independent of ambient temperature and the presence of NH₃ mitigation.

4. Conclusions

The formation potentials of secondary particles and O₃ from gasoline vehicle exhaust were examined at different temperatures with or without NH₃ mitigation. Among the total PM emitted, which included that produced by photochemical oxidation reactions, POA and EC accounted for only a small fraction, whereas the contribution of the secondary particles NH₄NO₃ and SOA was dominant. The yield of SOA was lower at lower temperatures. In a parameter sensitivity analysis, using a denuder to selectively reduce the concentration of NH₃ gas in the vehicle exhaust was found to have a marked effect on reducing the formation of NH₄NO₃ but not of SOA or O₃. Increased acidity (H⁺) was also observed with NH₃ mitigation. Overall, the present study highlights the importance of using photochemical smog chamber experiments to gain an informed understanding of the potential toxic effects and atmospheric and environmental impacts of vehicle emissions when implementing source control measures such as NH₃ emission limits.

Author Contributions: Conceptualization, H.H.; methodology, H.H.; validation, H.H.; investigation, H.H.; resources, H.H.; data curation, H.H. and R.U.; writing—original draft preparation, H.H.; writing—review and editing, H.H. and R.U.; visualization, H.H.; supervision, H.H.; project administration, H.H.; funding acquisition, H.H.

Funding: This study is a JARI internally funded Photochemical Smog Chamber Study for the Automotive Emissions Measurement Project.

Institutional Review Board Statement: Not applicable.

Informed Consent Statement: Not applicable.

Data Availability Statement: The data are not publicly available due to a confidentiality agreement with the part providers.

Acknowledgments: The authors would like to thank the co-workers who supported the set-up and operation of the dynamometer and the measurements. In addition, the authors would like to thank Dr. Akiyoshi Ito for his proofreading support during the preparation of the draft manuscript.

Conflicts of Interest: The authors declare no conflicts of interest.

References

1. Fujitani, Y.; Takahashi, K.; Saitoh, K.; Fushimi, A.; Hasegawa, S.; Kondo, Y.; Tanabe, K.; Takami, A.; Kobayashi, S. Contribution of industrial and traffic emissions to ultrafine, fine, coarse particles in the vicinity of industrial areas in Japan. *Environ. Adv.* **2021**, *5*, 100101. <https://doi.org/10.1016/j.envadv.2021.100101>
2. Achebak, H.; Garatachea, R.; Pay, M.T. Jorba, O.; Guevara, M.; García-Pando, C.P.; Ballester, J. Geographic sources of ozone air pollution and mortality burden in Europe. *Nat. Med.* **2024**, *30*, 1732–1738. <https://doi.org/10.1038/s41591-024-02976-x>
3. Fujitani, Y.; Furuyama, A.; Tanabe, K.; Hirano, S. Comparison of oxidative abilities of PM_{2.5} collected at traffic and residential sites in Japan. Contribution of transition metals and primary and secondary aerosols. *Aerosol Air Qual. Res.* **2017**, *17*, 574–587. <https://doi.org/10.4209/aaqr.2016.07.0291>
4. Shiraiwa, M.; Ueda, K.; Pozzer, A.; Lammel, G.; Kampf, C.J.; Fushimi, A.; Enami, S.; Arangio, A. M.; Frohlich-Nowoisky, J.; Fujitani, Y.; Furuyama, A.; Lakey, P.S.J.; Lelieveld, J.; Lucas, K.; Morino, Y.; Poschl, U.; Takahama, S.; Takami, A.; Tong, H.J.; Weber, B.; Yoshino, A.; Sato, K. Aerosol health effects from molecular to global scales. *Environ. Sci. Technol.* **2017**, *51*, 13545–13567. <https://doi.org/10.1021/acs.est.7b04417>
5. Künzi, L.; Krapf, M.; Daher, N.; Dommen, J.; Jeannet, N.; Schneider, S.; Platt, S.; Slowik, J. G.; Baumlin, N.; Salathe, M.; Prévôt, A.S.H.; Kalberer, M.; Strähl, C.; Dümbgen, L.; Sioutas, C.; Baltensperger, U.; Geiser.

M. Toxicity of aged gasoline exhaust particles to normal and diseased airway epithelia. *Sci Rep.* **2015**, *5*, 11801. <https://doi.org/10.1038/srep11801>

6. Lau, Y.S.; Poon, H.Y.; Organ, B.; Chuang, H.C.; Chan, M.-N.; Guo, H.; Ho, S.S.; Ho, K.-F. Toxicological effects of fresh and aged gasoline exhaust particles in Hong Kong. *J. Hazard Mater.* **2023**, *441*, 129846. <https://doi.org/10.1016/j.jhazmat.2022.129846>

7. Hayes, P.L.; Carlton, A.G.; Baker, K.R.; Ahmadov, R.; Washenfelder, R.A.; Alvarez, S.; Rappenglück, B.; Gilman, J.B.; Kuster, W.C.; de Gouw, J.A.; Zotter, P.; Prévôt, A.S.H.; Szidat, S.; Kleindienst, T.E.; Offenberg, J.H.; Ma, P.K.; Jimenez, J.L. Modeling the formation and aging of secondary organic aerosols in Los Angeles during CalNex 2010. *Atmos. Chem. Phys.* **2015**, *15*, 5773–5801. <https://doi.org/10.5194/acp-15-5773-2015>

8. Jathar, S.H.; Gordon, T.D.; Hennigan, C.J.; Pye, H.O.; Pouliot, G.; Adams, P.J.; Donahue, N.M.; Robinson, A.L. Unspeciated organic emissions from combustion sources and their influence on the secondary organic aerosol budget in the United States. *Proc. Natl. Acad. Sci. U.S.A.* **2014**, *111*, 10473–10478. <https://doi.org/10.1073/pnas.1323740111>

9. Jathar, S.H.; Woody, M.; Pye, H.O.T.; Baker, K.R.; Robinson, A.L. Chemical transport model simulations of organic aerosol in southern California: model evaluation and gasoline and diesel source contributions. *Atmos. Chem. Phys.* **2017**, *17*, 4305–4318. <https://doi.org/10.5194/acp-17-4305-2017>

10. Gentner, D.R.; Jathar, S.H.; Gordon, T.D.; Bahreini, R.; Day, D.A.; Haddad, I.E.; Haynes, P.L.; Pieber, S.M.; Platt, S.M.; De Gouw, J.; Goldstein, A.H.; Harley, R.A.; Jimenez, J.L.; Prevot, A.S.H.; Robinson, A.L. Review of urban secondary organic aerosol formation from gasoline and diesel motor vehicle emissions. *Environ. Sci. Technol.* **2017**, *51*, 1074–1093. <https://doi.org/10.1021/acs.est.6b04509>

11. Dunmore, R.E.; Hopkins, J.R.; Lidster, R.T.; Lee, J.D.; Evans, M.J.; Rickard, A.R.; Lewis, A.C.; Hamilton, J.F.; Diesel-related hydrocarbons can dominate gas phase reactive carbon in megacities, *Atmos. Chem. Phys.* **2015**, *15*, 9983–9996. <https://doi.org/10.5194/acp-15-9983-2015>

12. Platt, S.M.; El Haddad, I.; Pieber, M.; Zardini, A.A.; Suarez-Bertoa, R.; Clairotte, M.; Daellenbach, K.R.; Huang, R.J.; Slowik, J.G.; Hellebust, S.; et al. Gasoline cars produce more carbonaceous particulate matter than modern filter-equipped diesel cars. *Sci. Rep.* **2017**, *7*, 4926. <https://doi.org/10.1038/s41598-017-03714-9>

13. Nordin, E.Z.; Eriksson, A. C.; Roldin, P.; Nilsson, P.T.; Carlsson, J.E.; Kajos, M.K.; Hellén, H.; Wittbom, C.; Rissler, J.; Löndahl, J.; Swietlicki, E.; Svenssonsson, B.; Bohgard, M.; Kulmala, M.; Hallquist, M.; Pagels, J.H. Secondary organic aerosol formation from idling gasoline passenger vehicle emissions investigated in a smog chamber, *Atmos. Chem. Phys.* **2013**, *13*, 6101–6116. <https://doi.org/10.5194/acp-13-6101-2013>

14. Platt, S.M.; El Haddad, I.; Zardini, A.A.; Clairotte, M.; Astorga, C.; Wolf, R.; Slowik, J.G.; Temime-Roussel, B.; Marchand, N.; Ježek, I.; Drinovec, L.; Močnik, G.; Möhler, O.; Richter, R.; Barmet, P.; Bianchi, F.; Baltensperger, U.; Prévôt, A.S.H. Secondary organic aerosol formation from gasoline vehicle emissions in a new mobile environmental reaction chamber, *Atmos. Chem. Phys.* **2013**, *13*, 9141–9158. <https://doi.org/10.5194/acp-13-9141-2013>

15. Gordon, T.D.; Presto, A.A.; May, A.A.; Nguyen, N.T.; Lipsky, E.M.; Donahue, N.M.; Gutierrez, A.; Zhang, M.; Maddox, C.; Rieger, P.; Chattopadhyay, S.; Maldonado, H.; Maricq, M.M.; Robinson, A.L. Secondary organic aerosol formation exceeds primary particulate matter emissions for light-duty gasoline vehicles, *Atmos. Chem. Phys.* **2014**, *14*, 4661–4678. <https://doi.org/10.5194/acp-14-4661-2014>

16. Vu, D.; Roth, P.; Berte, T.; Yang, J.; Cocker, D.; Durbin, T.D.; Karavalakis, G.; Asa-Awuku, A. Using a new Mobile Atmospheric Chamber (MACH) to investigate the formation of secondary aerosols from mobile sources: The case of gasoline direct injection vehicles. *J. Aerosol Sci.* **2019**, *133*, 1–11. <https://doi.org/10.1016/j.jaerosci.2019.03.009>

17. Zhao, Y.; Saleh, R.; Saliba, G.; Presto, A.A.; Gordon, T.D.; Drozd, G.T.; Goldstein, A.H.; Donahue, N.M.; Robinson, A.L. Reducing secondary organic aerosol formation from gasoline vehicle exhaust. *Proc. Natl. Acad. Sci. U.S.A.* **2017**, *114*, 6984–6989. <https://doi.org/10.1073/pnas.1620911114>

18. Morino, Y.; Li, Y.; Fujitani, Y.; Sato, K.; Inomata, S.; Tanabe, K.; Jathar, S.H.; Kondo, Y.; Nakayama, T.; Fushimi, A.; Takami, A.; Kobayashi, S. Secondary organic aerosol formation from gasoline and diesel vehicle exhaust under light and dark conditions. *Environ. Sci. Atmos.* **2022**, *46*–64. <https://doi.org/10.1039/D1EA00045D>

19. Liu, T.; Wang, X.; Deng, W.; Hu, Q.; Ding, X.; Zhang, Y.; He, Q.; Zhang, Z.; Lü, S.; Bi, X.; Chen, J., and Yu, J.: Secondary organic aerosol formation from photochemical aging of light-duty gasoline vehicle exhausts in a smog chamber. *Atmos. Chem. Phys.* **2015**, *15*, 9049–9062, <https://doi.org/10.5194/acp-15-9049-2015>

20. Pieber, S.M.; Kumar, N.K.; Klein, F.; Comte, P.; Bhattu, D.; Dommen, J.; Bruns, E.A.; Kılıç, D.; El Haddad, I.; Keller, A.; Czerwinski, J.; Heeb, N.; Baltensperger, U.; Slowik, J.G.; Prévôt, A.S.H. Gas-phase composition and secondary organic aerosol formation from standard and particle filter-retrofitted gasoline direct injection vehicles investigated in a batch and flow reactor, *Atmos. Chem. Phys.* **2018**, *18*, 9929–9954. <https://doi.org/10.5194/acp-18-9929-2018>

21. Roth, P.; Yang, J.; Fofie, E.; Cocker, D.R.; Durbin, T.D.; Brezny, R.; Geller, M.; Asa-Awuku, A.; Karavalakis, G. Catalyzed gasoline particulate filters reduce secondary organic aerosol production from gasoline direct injection vehicles. *Environ. Sci. Technol.* **2019**, *53*, 3037–3047. <https://doi.org/10.1021/acs.est.8b06418>

22. Drozd, G.T.; Zhao, Y.; Saliba, G.; Frodin, B.; Maddox, C.; Oliver Chang, M.C.; Maldonado, H.; Sardar, S.; Weber, R.J.; Robinson, A.L.; et al. Detailed speciation of intermediate volatility and semivolatile organic compound emissions from gasoline vehicles: effects of cold-starts and implications for secondary organic aerosol formation. *Environ. Sci. Technol.*, **2019**, *53*, 1706–1714. <https://doi.org/10.1021/acs.est.8b05600>

23. Karjalainen, P.; Timonen, H.; Saukko, E.; Kuuluvainen, H.; Saarikoski, S.; Aakko-Saksa, P.; Murtonen, T.; Bloss, M.; Dal Maso, M.; Simonen, P.; Ahlberg, E.; Svenningsson, B.; Brune, W.H.; Hillamo, R.; Keskinen, J.; Rönkkö, T. Time-resolved characterization of primary particle emissions and secondary particle formation from a modern gasoline passenger car, *Atmos. Chem. Phys.*, **2016**, *16*, 8559–8570, <https://doi.org/10.5194/acp-16-8559-2016>, 2016.

24. Suarez-Bertoa, R.; Zardini, A. A.; Platt, S. M.; Hellebust, S.; Pieber, S. M.; El Haddad, I.; Temime-Roussel, B.; Baltensperger, U.; Marchand, N.; Prévôt, A. S. H.; Astorga, C. Primary Emissions and Secondary Organic Aerosol Formation from the Exhaust of a Flex-Fuel (Ethanol) Vehicle. *Atmos. Environ.* **2015**, *117*, 200–211, <https://doi.org/10.1016/j.atmosenv.2015.07.006>

25. Roth, P.; Yang, J.; Peng, W.; Cocker III, D.R.; Durbin, T.D.; Asa-Awuku, A.; Karavalakis, G. Intermediate and high ethanol blends reduce secondary organic aerosol formation from gasoline direct injection vehicles. *Atmos. Environ.* **2020**, *220*, 117064.

26. Hui Wang, Song Guo, Ying Yu, Ruizhe Shen, Wenfei Zhu, Rongzhi Tang, Rui Tan, Kefan Liu, Kai Song, Wenbin Zhang, Zhou Zhang, Shijin Shuai, Hongming Xu, Jing Zheng, Shiyi Chen, Shaomeng Li, Limin Zeng, Zhijun Wu. Secondary aerosol formation from a Chinese gasoline vehicle: Impacts of fuel (E10, gasoline) and driving conditions (idling, cruising). *Science of The Total Environment* **2021**, *795*, 148809. <https://doi.org/10.1016/j.scitotenv.2021.148809>

27. Hartikainen, A., Ihälainen, M., Yli-Pirila, P., Hao, L., Kortelainen, M., Pieber, S., and Sippula, O.: Photochemical Transformation and Secondary Aerosol Formation Potential of Euro6 Gasoline and Diesel Passenger Car Exhaust Emissions, *J. Aerosol Sci.* **2023**, *171*, 106159, <https://doi.org/10.1016/j.jaerosci.2023.106159>

28. Naomi J. Farren, Jack Davison, Rebecca A. Rose, Rebecca L. Wagner, and David C. Carslaw. Underestimated ammonia emissions from road vehicles. *Environ. Sci. Technol.*, **2020**, *54* (24), 15689–15697. <https://doi.org/10.1021/acs.est.0c05839>

29. Suarez-Bertoa, R.; Zardini, A.A.; Astorga, C. Ammonia exhaust emissions from spark ignition vehicles over the New European Driving Cycle. *Atmos. Environ.*, **2014**, *97*, 43–53. <https://doi.org/10.1016/j.atmosenv.2014.07.050>

30. Bajwa, A.; Shankar, V.; Leach, F. Ammonia emissions from combustion in gasoline engines, SAE Technical Paper 2023-01-1655, **2023**, <https://doi.org/10.4271/2023-01-1655>.

31. Kaltsonoudis, C.; Jorga, S.D.; Louvaris, E.; Florou, K.; Pandis, S.N. A portable dual-smog-chamber system for atmospheric aerosol field studies. *Atmos. Meas. Tech.* **2019**, *12*, 2733–2743. <https://doi.org/10.5194/amt-12-2733-2019>

32. Kelly, N.A. Characterization of Fluorocarbon-Film Bags as Smog Chambers. *Environ. Sci. Technol.*, **1982**, *16*, *11*, 763–770. <https://doi.org/10.1021/es00105a007>

33. Paulsen, D., Dommen, J., Kalberer, M., Prevot, A. S. H., Richter, R., Sax, M., Steinbacher, M., Weingartner, E., and Baltensperger, U.: Secondary organic aerosol formation by irradiation of 1,3,5- trimethylbenzene-NOx-H₂O in a new reaction chamber for atmospheric chemistry and physics, *Environ. Sci. Technol.*, **2005**, *39*, 2668–2678. <https://pubs.acs.org/doi/10.1021/es0489137>

34. Wang, X., Liu, T., Bernard, F., Ding, X., Wen, S., Zhang, Y., Zhang, Z., He, Q., Lü, S., Chen, J., Saunders, S., and Yu, J.: Design and characterization of a smog chamber for studying gas-phase chemical mechanisms and aerosol formation, *Atmos. Meas. Tech.*, **2014**, *7*, 301–313, <https://doi.org/10.5194/amt-7-301-2014>

35. Peng, J., Hu, M., Du, Z., Wang, Y., Zheng, J., Zhang, W., Yang, Y., Qin, Y., Zheng, R., Xiao, Y., Wu, Y., Lu, S., Wu, Z., Guo, S., Mao, H., and Shuai, S.: Gasoline aromatics: a critical determinant of urban secondary organic aerosol formation, *Atmos. Chem. Phys.* **2017**, *17*, 10743–10752, <https://doi.org/10.5194/acp-17-10743-2017>

36. Carter, W.P.; Cockeriii, D.R., III; Fitz, D.R.; Malkina, I.L.; Bumiller, K.; Sauer, C.G.; Pisano, J.; Bufalino, C.; Song, C. A new environmental chamber for evaluation of gas-phase chemical mechanisms and secondary aerosol formation. *Atmos. Environ.*, **2005**, *39*, 7768–7788. <https://doi.org/10.1016/j.atmosenv.2005.08.040>

37. Atkinson, R., Baulch, D. L., Cox, R. A., Crowley, J. N., Hampson, R. F., Hynes, R. G., Jenkin, M. E., Rossi, M. J., and Troe, J.: Evaluated kinetic and photochemical data for atmospheric chemistry: Volume I - gas phase reactions of Ox, HOx, NOx and SOx species, *Atmos. Chem. Phys.*, **2004**, *4*, 1461–1738. <https://doi.org/10.5194/acp-4-1461-2004>

38. Atkinson, R. Arey, J. atmospheric degradation of volatile organic compounds, *Chem. Rev.* **2003**, *4605–4638*. <https://doi.org/10.1021/cr0206420>

39. William P.L. Carter. Development of the SAPRC-07 chemical mechanism. *Atmos. Environ.*, **2010**, *44*, 5324–5335. <https://doi.org/10.1016/j.atmosenv.2010.01.026>

40. Nenes, A.; Pandis S.N.; Pilinis, C. ISORROPIA: A new thermodynamic equilibrium model for multiphase multicomponent inorganic aerosols. *Aquat. Geoch.*, **1998**, *4*, 123-152. <https://doi.org/10.1023/A:1009604003981>

41. Xing, J., Shao, L., Zhang, W., Peng, J., Wang, W., Shuai, S., Hu, M., and Zhang, D.: Morphology and size of the particles emitted from a gasoline-direct-injection-engine vehicle and their ageing in an environmental chamber, *Atmos. Chem. Phys.* **2020**, *20*, 2781–2794. <https://doi.org/10.5194/acp-20-2781-2020>

42. McMurry, P.H.; Grosjean, D. Gas and Aerosol Wall Losses in Teflon Film Smog Chambers, *Environ. Sci. Technol.* **1985**, *19*, 1176–1182. <https://doi.org/10.1021/es00142a006>

43. Mendoza, D.L.; Hill, L.D.; Blair, J.; Crozman, E.T. A Long-Term Comparison between the AethLabs MA350 and Aerosol Magee Scientific AE33 Black Carbon Monitors in the Greater Salt Lake City Metropolitan Area. *Sensors* **2024**, *24*, 965. <https://doi.org/10.3390/s24030965>

44. Cocker, D.; Flagan, R.; Seinfeld, J. State-of-the-art chamber facility for studying atmospheric aerosol chemistry. *Environ. Sci. Technol.* **2001**, *35*, 2594–2601. <https://doi.org/10.1021/es0019169>

45. Gordon, T.D.; Presto, A.A.; Nguyen, N.T.; Robertson, W.H.; Na, K.; Sahay, K.N.; Zhang, M.; Maddox, C.; Rieger, P.; Chattopadhyay, S.; et al. Secondary Organic Aerosol Production from Diesel Vehicle Exhaust: Impact of Aftertreatment, Fuel Chemistry and Driving Cycle. *Atmos. Meas. Tech.* **2014**, *14*, 4643–4659. <https://doi.org/10.5194/acp-14-4643-2014>

46. Pang, Y.; Turpin, B. J.; Gundel, L. A. On the Importance of Organic Oxygen for Understanding Organic Aerosol Particles. *Aerosol Sci. Technol.* **2006**, *40*, 128–133. <https://doi.org/10.1080/02786820500423790>

47. Aiken, A.C.; DeCarlo, P.F.; Jimenez, J.L. Elemental Analysis of Organic Species with Electron Ionization High-Resolution Mass Spectrometry. *Anal. Chem.* **2007**, *79*, 8350–8358. <https://doi.org/10.1021/ac071150w>

48. Aiken, A.C.; DeCarlo, P.F.; Kroll, J.H.; Worsnop, D.R.; Huffman, J.A.; Docherty, K.S.; Ulbrich, I.M.; Mohr, C.; Kimmel, J.R.; Sueper, D.; Sun, Y.; Zhang, Q.; Trimborn, A.; Northway, M.; Ziemann, P.J.; Canagaratna, M.R.; Onasch, T.B.; Alfarra, M.R.; Prevot, A.S.H.; Dommen, J.; Duplissy, J.; Metzger, A.; Baltensperger, U.; Jimenez, J.L. O/C and OM/OC Ratios of Primary, Secondary, and Ambient Organic Aerosols with High-Resolution Time-of-Flight Aerosol Mass Spectrometry. *Environ. Sci. Technol.* **2008**, *42*, 4478–4485. <https://doi.org/10.1021/es703009q>

49. Hayes P.L.; Ortega, A.M.; Cubison, M.J.; Froyd, K.D.; Zhao, Y.; Cliff, S.S.; Hu, W.W.; Toohey, D.W.; Flynn, J.H.; Lefer, B.L.; Grossberg, N.; Alvarez, S.; Rappenglück, B.; Taylor, J.W.; Allan, J.D.; Holloway, J.S.; Gilman, J.B.; Kuster, W.C.; de Gouw, J.A.; Massoli, P.; Zhang, X.; Liu, J.; Weber, R.J.; Corrigan, A.L.; Russell, L.M.; Isaacman, G.; Worton, D.R.; Kreisberg, N.M.; Goldstein, A.H.; Thalman, R.; Waxman, E.M.; Volkamer, R.; Lin, Y.H.; Surratt, J.D.; Kleindienst, T.E.; Offenberg, J.H.; Dusanter, S.; Griffith, S.; Stevens, P.S.; Brioude, J.; Angevine, W.M.; Jimenez, J.L. Organic Aerosol Composition and Sources in Pasadena, California, during the 2010 CalNex Campaign. *J. Geophys. Res. Atmos.* **2013**, *118*:9233–9257. <https://doi.org/10.1002/jgrd.50530>

50. Park G, Kim K, Park T, Kang S, Ban J, Choi S, et al. Primary and Secondary Aerosols in Small Passenger Vehicle Emissions: Evaluation of Engine Technology, Driving Conditions, and Regulatory Standards. *Environ. Pollut.* **2021**, *286*, 117195. <https://doi.org/10.1016/j.envpol.2021.117195>

51. Nakamura, K.; Dardiotis, C.; Kandlhofer, C.; Arndt, M. Challenges related to the measurement of particle emissions of gasoline direct injection engines under cold-start and low-temperature conditions. *Int. J. Auto. Eng.*, **2019**, *10*, 332–339. https://doi.org/10.20485/jxaeijae.10.4_332

52. Yang, J.; Roth, P.; Durbin, T. D.; Johnson, K. C.; Cocker, D. R., III; Asa-Awuku, A.; Brezny, R.; Geller, M.; Karavalakis, G. Gasoline particulate filters as an effective tool to reduce particulate and PAH emissions from GDI vehicles: A case study with two GDI vehicles. *Environ. Sci. Technol.* **2018**, *52*, 3275–3284. <https://pubs.acs.org/doi/abs/10.1021/acs.est.7b05641>

53. Calvert, J.G.; Stockwell, W.R. Acid generation in the troposphere by gas-phase chemistry. *Environ. Sci. Technol.*, **1983**, *17*, pp. 428A–443A. <https://pubs.acs.org/doi/10.1021/es00115a002>

54. Stockwell, W.R.; Kirchner, F.; Kuhn, M.; Seefeld, S. A new mechanism for regional atmospheric chemistry modeling. *J. Geophys. Res.-Atmos.*, **1997**, *102*, 25847–25879. <https://doi.org/10.1029/97JD00849>

55. Geyer, A.; Aliche, B.; Ackermann, R.; Martinez, M.; Harder, H.; Brune, W.; Carlo, P. di; Williams, E.; Jobson, T.; Hall, S.; Shetter, R.; Stutz, J. Direct observations of daytime NO_3 . Implications for urban boundary layer chemistry, *J. Geophys. Res.-Atmos.*, **2003**, *108*, 4368. <https://doi.org/10.1029/2002JD002967>

56. Brown, S.S.; Osthoff, H.D.; Stark, H.; Dubé, W.P.; Ryerson, T.B.; Warneke, C.; de Gouw, J.A.; Wollny, A.G.; Parrish, D.D.; Fehsenfeld, F.C.; Ravishankara, A.R. Aircraft observations of daytime NO_3 and N_2O_5 and their implications for tropospheric chemistry. *J. Photochem. Photobiol. A Chem.*, **2005**, *176*, 270–278. <https://doi.org/10.1016/j.jphotochem.2005.10.004>

57. Osthoff, H.D.; Sommariva, R.; Baynard, T.; Pettersson, A.; Williams, E.J.; Lerner, B.M.; Roberts, J.M.; Stark, H.; Goldan, P.D.; Kuster, W.C.; Bates, T.S.; Coffman, D.; Ravishankara, A.R.; Brown, S.S. Observation of daytime N_2O_5 in the marine boundary layer during New England Air Quality Study–Intercontinental Transport and Chemical Transformation 2004, *J. Geophys. Res.-Atmos.*, **2006**, *111*, D23S14. <https://doi.org/10.1029/2006JD007593>

58. Meng, Z.; Dabdub, D.; Seinfeld, J.H. Chemical coupling between atmospheric ozone and particulate matter. *Science*, **1997**, 277, 116–119. <https://doi.org/10.1126/science.277.5322.116>

59. Stelson, A.W.; Seinfeld, J.H.; Thermodynamic prediction of the water activity, NH_4HO_3 dissociation constant, density and refractive index for the $\text{NH}_4\text{NO}_3\text{--}(\text{NH}_4)_2\text{SO}_4\text{H}_2\text{O}$ system at 25°C. *Atmos. Environ.*, **1982**, 16, 2507–2514. [https://doi.org/10.1016/0004-6981\(82\)90142-1](https://doi.org/10.1016/0004-6981(82)90142-1)

60. Stelson, A.W.; Seinfeld, J.H. Relative humidity and temperature dependence of the ammonium nitrate dissociation constant. *Atmos. Environ.*, **1982**, 16, 983–992. [https://doi.org/10.1016/0004-6981\(82\)90184-6](https://doi.org/10.1016/0004-6981(82)90184-6)

61. Stelson, A.W.; Seinfeld, J.H. Relative humidity and pH dependence of the vapor pressure of ammonium nitrate–nitric acid solutions at 25 degrees C. *Atmos. Environ.*, **1982**, 16, 993–1000. [https://doi.org/10.1016/0004-6981\(82\)90185-8](https://doi.org/10.1016/0004-6981(82)90185-8)

62. Gong, J.; Rutland, C. Three way catalyst modeling with ammonia and nitrous oxide kinetics for a lean burn spark ignition direct injection (SIDI) gasoline engine. *SAE Tech. Pap. Ser.*, **2013**, 2013-01-1572. <https://doi.org/10.4271/2013-01-1572>

63. Heeb, N.V.; Forss, A.M.; Bruhlmann, S.; Luscher, R.; Sacher, C. J.; Hug, P. Three-way catalyst-induced formation of ammonia-velocity and acceleration-dependent emission factors. *Atmos. Environ.*, **2006**, 40, 5986–5997. <https://doi.org/10.1016/j.atmosenv.2005.12.035>

64. Gandhi, H.S.; Graham, G.W.; McCabe, R.W. Automotive exhaust catalysis. *J. Catal.*, **2003**, 216, 433–442. [https://doi.org/10.1016/S0021-9517\(02\)00067-2](https://doi.org/10.1016/S0021-9517(02)00067-2)

65. Schlatter, J.C.; Taylor, K.C. Platinum and palladium addition to supported rhodium catalysts for automotive emission control. *J. Catal.*, **1977**, 49, 42–50. [https://doi.org/10.1016/0021-9517\(77\)90238-X](https://doi.org/10.1016/0021-9517(77)90238-X)

66. Kobylinski, T.P.; Taylor, B.W. The catalytic chemistry of nitric oxide: II. Reduction of nitric oxide over noble metal catalysts. *J. Catal.*, **1974**, 33 (1974), 376–384. [https://doi.org/10.1016/0021-9517\(74\)90284-X](https://doi.org/10.1016/0021-9517(74)90284-X)

67. Renème, Y.; Dhainaut, F.; Granger, P. Kinetics of the $\text{NO}/\text{H}_2/\text{O}_2$ reactions on natural gas vehicle catalysts—Influence of Rh addition to Pd. *Appl. Catal. B Environ.*, **2012**, 111–112, pp. 424–432. <https://doi.org/10.1016/j.apcatb.2011.10.030>

68. Na, K.; Song, C.; Switzer, C.; Cocker, D.R. Effect of ammonia on secondary organic aerosol formation from α -pinene ozonolysis in dry and humid conditions. *Environ. Sci. Technol.*, **2007**, 41, 6096–6102. <https://doi.org/10.1021/es061956y>

69. Na, K.; Song, C.; Cocker, D.R. Formation of secondary organic aerosol from the reaction of styrene with ozone in the presence and absence of ammonia and water. *Atmos. Environ.*, **2006**, 40, 1889–1900. <https://doi.org/10.1016/j.atmosenv.2005.10.063>

70. Qiao, M.; Xiaoxiao, L.; Chengqiang, Y.; Bo, L.; Yanbo, G.; Weijun, Z. The influences of ammonia on aerosol formation in the ozonolysis of styrene: roles of Criegee intermediate reactions. *R. Soc. Open Sci.*, **2018**, 5172171. <https://doi.org/10.1098/rsos.172171>

71. McDonald, B.C.; de Gouw, J.A.; Gilman, J.B.; Jathar, S.H.; Akherati, A.; Cappa, C.D.; Jimenez, J.L.; Lee-Taylor, J.; Hayes, P.L.; McKeen, S.A.; Cui, Y.Y.; Kim, S.-W.; Gentner, D.R.; Isaacman-Vanwertz, G.; Goldstein, A.H.; Harley, R.A.; Frost, G.J.; Roberts, J.M.; Ryerson, T.B.; Trainer, M. Volatile chemical products emerging as largest petrochemical source of urban organic emissions. *Science*, **2018**, 359760–764 doi: 10.1126/science.aaq0524

72. Srivastava, D.; Vu, T.V.; Tong, S.; Shi, Z.; Harrison, R.M. Formation of secondary organic aerosols from anthropogenic precursors in laboratory studies. *npj Clim. Atmos. Sci.*, **2022**, 5, 22. <https://doi.org/10.1038/s41612-022-00238-6>

73. Pankow, J.F.: An absorption-model of gas-particle partitioning of organic compounds in the atmosphere, *Atmos. Environ.*, **1994**, 28, 185–188. [https://doi.org/10.1016/1352-2310\(94\)90093-0](https://doi.org/10.1016/1352-2310(94)90093-0)

74. Pankow, J.F.: An absorption-model of the gas aerosol partitioning involved in the formation of secondary organic aerosol, *Atmos. Environ.*, **1994**, 28, 189–193. [https://doi.org/10.1016/1352-2310\(94\)90094-9](https://doi.org/10.1016/1352-2310(94)90094-9)

75. Odum, J.R.; Jungkamp, T.P.W.; Griffin, R.J.; Forstner, H.J.L.; Flagan, R.C.; Seinfeld, J.H. Aromatics, reformulated gasoline, and atmospheric organic aerosol formation. *Environ. Sci. Technol.*, **1997**, 31, 1890–1897. <https://doi.org/10.1021/es960535l>

76. Takekawa, H., Minoura, H., and Yamazaki, S. Temperature Dependence of Secondary Organic Aerosol Formation by Photo-Oxidation of Hydrocarbons. *Atmos. Environ.*, **2003**, 37, 3413–3424. [https://doi.org/10.1016/S1352-2310\(03\)00359-5](https://doi.org/10.1016/S1352-2310(03)00359-5)

77. Svendby, T.M.; Lazaridis, M.; Tørseth, K. Temperature dependent secondary organic aerosol formation from terpenes and aromatics. *J. Atmos. Chem.*, **2008**, 59, 25–46. <https://doi.org/10.1007/s10874-007-9093-7>

78. Bao, Z.E.; Xu, H.F.; Li, K.W.; Chen, L.H.; Zhang, X.; Wu, X.C.; Gao, X.; Azzi, M.; Cen, K.F. Effects of NH_3 on secondary aerosol formation from toluene/ NO_x photo-oxidation in different O_3 formation regimes. *Atmos. Environ.*, **2021**, 261, 11. <https://doi.org/10.1016/j.atmosenv.2021.118603>

79. Carter, W.P.L.; Atkinson, R. Computer modeling study of incremental hydrocarbon reactivity, *Environ. Sci. Technol.*, **1989**, 23, 864–880. <https://doi.org/10.1021/es00065a017>

80. Chang, T.Y.; Rudy, S.J. Ozone-forming potential of organic emissions from alternative-fueled vehicles. *Atmos. Environ.*, **1990**, 24, 2421–2430. [https://doi.org/10.1016/0960-1686\(90\)90335-K](https://doi.org/10.1016/0960-1686(90)90335-K)

81. Carter, W.P.L. Development of ozone reactivity scales for volatile organic compounds, *J. Air Waste Manage.*, **1994**, *44*, 881–899. <https://doi.org/10.1080/1073161X.1994.10467290>
82. Venecek, M.A.; Carter, W.P.L.; Kleeman, M.J. Updating the SAPRC maximum incremental reactivity (MIR) scale for the United States from 1988 to 2010. *J. Air Waste Manage.*, **2018**, *68*, 1301–1316, <https://doi.org/10.1080/10962247.2018.1498410>
83. Zhang, Y.; Xue, L.; Carter, W.P.L.; Pei, C.; Chen, T.; Mu, J.; Wang, Y.; Zhang, Q.; Wang, W. Development of ozone reactivity scales for volatile organic compounds in a Chinese megacity. *Atmos. Chem. Phys.*, **2021**, *21*, 11053–11068. <https://doi.org/10.5194/acp-21-11053-2021>
84. Yamada, H.; Inomata, S.; Tanimoto, H. Refueling emissions from cars in Japan: Compositions, temperature dependence and effect of vapor liquefied collection system. *Atmos. Environ.* **2015**, *120*, 455– 462. <https://doi.org/10.1016/j.atmosenv.2015.09.026>
85. Yamada, H.; Inomata, S.; Tanimoto, H.; Hata, H.; Tonokura, K. Estimation of refueling emissions based on theoretical model and effects of E10 fuel on refueling and evaporative emissions from gasoline cars. *Sci. Total Environ.* **2018**, *622*, 467–473. <https://doi.org/10.1016/j.scitotenv.2017.11.339>
86. Black, F.; Tejada, S.; Gurevich, M. Alternative fuel motor vehicle tailpipe and evaporative emissions composition and ozone potential. *J. Air & Waste Manag. Assoc.*, **1998**, *48*, 578–591. <https://doi.org/10.1080/10473289.1998.10463715>
87. Kajima, K.; Hirota, T.; Yakushiji, K.; Iwakiri, Y.; Oda, K.; Akutsu, Y. Effect of reformulated gasoline and methanol on exhaust emissions. *SAE Technical Paper 912431*, **1991**. <https://doi.org/10.4271/912431>.
88. Hata, H.; Okada, M.; Funakubo, C.; Hoshi, J. Tailpipe VOC Emissions from late model gasoline passenger vehicles in the Japanese market. *Atmosphere* **2019**, *10*, 621. <https://doi.org/10.3390/atmos10100621>
89. Carter, W.P.L.; Heo, G. Development of revised SAPRC aromatics mechanisms. Report to the California Air Resources Board Contracts No. 07-730 and 08-326, April 12, 2012. Available at <https://intra.enrgr.ucr.edu/~carter/SAPRC/scales11.xls>
90. Carter, W.P.L.; Heo, G. Development of revised SAPRC aromatic mechanisms. *Atmos. Environ.*, **2013**, *77*, 404–414. <https://doi.org/10.1016/j.atmosenv.2013.05.021>

Disclaimer/Publisher's Note: The statements, opinions and data contained in all publications are solely those of the individual author(s) and contributor(s) and not of MDPI and/or the editor(s). MDPI and/or the editor(s) disclaim responsibility for any injury to people or property resulting from any ideas, methods, instructions or products referred to in the content.